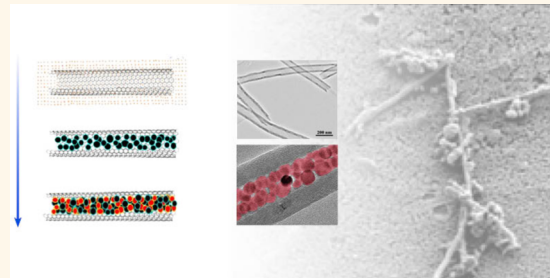


Design of Covalently Functionalized Carbon Nanotubes Filled with Metal Oxide Nanoparticles for Imaging, Therapy, and Magnetic Manipulation

Xiaojie Liu,^{†,‡,||} Iris Marangon,^{§,||} Georgian Melinte,[‡] Claire Wilhelm,[§] Cécilia Ménard-Moyon,[⊥] Benoit P. Pichon,[‡] Ovidiu Ersen,[‡] Kelly Aubertin,[§] Walid Baaziz,[†] Cuong Pham-Huu,[†] Sylvie Bégin-Colin,^{*,‡} Alberto Bianco,^{*,⊥} Florence Gazeau,^{*,§} and Dominique Bégin^{*,†}

[†]Institut de Chimie et Procédés pour l'Energie, l'Environnement et la Santé (ICPEES), UMR-7515 CNRS-Université de Strasbourg, 25 rue Becquerel, 67087 Strasbourg Cedex 2, France, [‡]Institut de Physique et Chimie des Matériaux de Strasbourg (IPCMS), UMR-7504 CNRS-Université de Strasbourg, 23 rue du Loess, BP 34 67034 Strasbourg Cedex 2, France, [§]Laboratoire Matière et Systèmes Complexes (MSC), UMR-7057 CNRS-Université Paris-Diderot, PRES Sorbonne Paris Cité, 75205 Paris Cedex 13, France, and [⊥]CNRS, Institut de Biologie Moléculaire et Cellulaire, Laboratoire d'Immunopathologie et Chimie Thérapeutique, UPR 3572, 67000 Strasbourg, France. ^{||}These authors contributed equally.

ABSTRACT Nanocomposites combining multiple functionalities in one single nano-object hold great promise for biomedical applications. In this work, carbon nanotubes (CNTs) were filled with ferrite nanoparticles (NPs) to develop the magnetic manipulation of the nanotubes and their theranostic applications. The challenges were both the filling of CNTs with a high amount of magnetic NPs and their functionalization to form biocompatible water suspensions. We propose here a filling process using CNTs as nanoreactors for high-yield *in situ* growth of ferrite NPs into the inner carbon cavity. At first, NPs were formed inside the nanotubes by thermal decomposition of an iron stearate precursor. A second filling step was then performed with iron or cobalt stearate precursors to enhance the encapsulation yield and block the formed NPs inside the tubes. Water suspensions were then obtained by addition of amino groups *via* the covalent functionalization of the external surface of the nanotubes. Microstructural and magnetic characterizations confirmed the confinement of NPs into the anisotropic structure of CNTs making them suitable for magnetic manipulations and MRI detection. Interactions of highly water-dispersible CNTs with tumor cells could be modulated by magnetic fields without toxicity, allowing control of their orientation within the cell and inducing submicron magnetic stirring. The magnetic properties were also used to quantify CNTs cellular uptake by measuring the cell magnetophoretic mobility. Finally, the photothermal ablation of tumor cells could be enhanced by magnetic stimulus, harnessing the hybrid properties of NP loaded-CNTs.



KEYWORDS: magnetic carbon nanotubes · functionalization · iron oxide nanoparticles · cobalt oxide nanoparticles · filling · magnetic core–shell nanoparticles · MRI · hyperthermia · cell interactions

The design of metal oxide nanoparticles and their association with other nanomaterials to yield composites which combine properties of both entities is currently a subject in full development due to their wide range of potential applications (electronic and magnetic devices, data and energy storage, and theranostic vectors).^{1–9}

Among such nanocomposites, there is currently intense interest in associating carbon nanotubes with metal oxide NPs in order to exploit the unique properties of

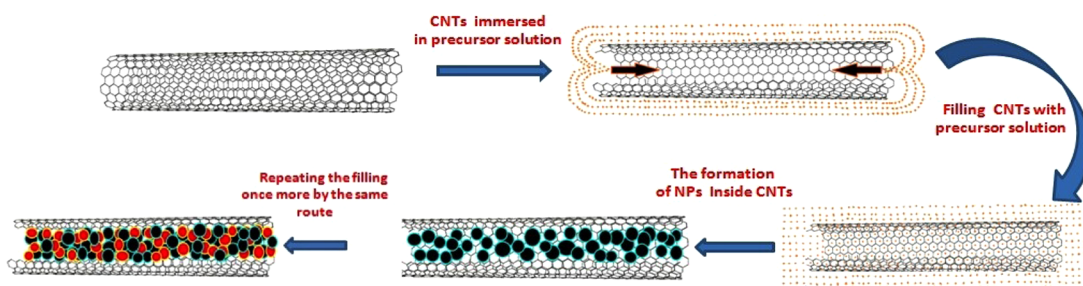
each material: electrical and thermal conductivities, architectural and mechanical properties of CNTs, and magnetic properties and chemical stability of metal oxides NPs. In particular, super-paramagnetic iron oxide nanoparticles (SPIONs) have been widely developed in the biomedical field as MRI contrast agents and heat mediators for cancer hyperthermia, cell sorting, drug delivery, immunoassay, and tissue repair.^{10,11} Similarly, CNTs are promising for biomedical applications as they are able to cross many biological and biophysical barriers with minimal

* Address correspondence to dominique.beguin@unistra.fr, a.bianco@ibmc-cnrs.unistra.fr, florence.gazeau@univ-paris-diderot.fr, sylvie.beguin@ipcms.unistra.fr.

Received for review July 23, 2014 and accepted October 24, 2014.

Published online October 24, 2014
10.1021/nn5040923

© 2014 American Chemical Society



Scheme 1. Schematic Presentation of the Two-Step Filling Process Enhancing the Filling of CNTs by Metal Oxide NPs

cytotoxic effects.¹² Both single-walled (SWCNTs) and multiwalled CNTs (MWCNTs) have unique properties which make them suitable for applications in a variety of imaging modalities, such as near-infrared fluorescence, Raman spectroscopy, photoacoustic tomography, and ultrasonography.^{13–18} Furthermore, CNTs possess a very broad absorbance spectrum, also covering the near-infrared (NIR) optical transmission window where biological tissues are transparent.¹⁹ Following exposure to NIR light, CNTs enter an excited state and release vibrational energy that is transformed into heat. In contrast to plasmonic nanoheaters such as gold nanorods or nanoshells, the energy transduction efficiency of CNTs is less dependent on particle characteristics and excitation wavelengths. Iron oxide nanoparticles and CNTs have also been recently reported as near-infrared photothermal agents for tumor ablation.^{20,21} Therefore, designing nanohybrids combining complementary functionalities of CNTs and nanomagnets should lead to promising nano-objects for theranostic applications. The real challenge is, however, to preserve the unique properties of each component once associated and to make the nanocomposites dispersible and compatible with biological media. Most recent attempts have led to the decoration of CNTs with magnetic nanoparticles on their outer layer. Although the nanohybrids could serve for MRI monitoring of CNTs,^{16,22,23} the surface decoration changes the surface properties of nanotubes and does not lead to magnetically anisotropic structures. Another strategy is thus to fill the empty channel of CNTs with magnetic materials in order to obtain anisotropic nanomagnets embedded into the carbon template. It has been recently shown that according to the nature of the CNT surface, NPs could be incorporated preferentially outside or inside their channel.^{24–27} In particular, it has been demonstrated that the encapsulation of NPs prevented them from oxidation and enhanced their chemical inertness. Indeed, cobalt-based NPs were encapsulated into CNTs, and the chemical characterizations have shown a relatively high Co/O atomic ratio. This indicates that the surface oxidation remains relatively low in CNT-embedded cobalt NPs in comparison to free NPs,²⁶ but the filling of CNTs with high efficiency, high density, and high stability has not been

achieved so far. Electrochemical methods,²⁸ direct incorporation of iron during the MWCNTs synthesis^{29–31} or magnetic capillary technique,^{32,33} or more frequently, CNT filling with liquid salt by capillary effect have been investigated.³⁴ These approaches were generally followed by a suitable thermal treatment to obtain the desired NPs.^{35,36} The incipient wetness impregnation is the most adapted method to control the filling yield.^{37,38} We recently proposed an alternative method to fill MWCNTs with iron oxide or cobalt-based NPs in one step under soft conditions: the synthesis of NPs by thermal decomposition of the metal precursor is induced inside CNTs, which act as nanoreactors.^{26,27} The size and the morphology of the NPs were very homogeneous and were found to depend on the nature of the metal precursor and on the MWCNT internal diameter. Cobalt stearate precursor led to large octahedral NPs which occupied the whole volume of CNTs, and they were blocked inside the CNTs.²⁶ Despite their high filling density, iron oxide NPs inside CNTs display smaller diameters than the CNTs diameter (like peas in peapods), and then they tend to slide outside CNTs when they are purified and further manipulated.²⁷ Thus, the filling density and the blocking of NPs inside CNTs has to be improved to envision multifunctional magnetic CNTs efficient for biomedical applications. Here, a double-filling process involving the thermal decomposition of either iron and/or cobalt stearate precursors inside CNTs has been developed in order to increase the filling rate and block the NPs inside CNTs. Such a process led to enhanced filling density and provided magnetic CNTs manipulable by an external magnetic field (Scheme 1). These magnetic CNTs have been functionalized to ensure their dispersibility in physiological media. For the first time, magnetic CNTs could be handled when interacting with cancer cells for controlling CNT orientation within the cell without toxicity. Such nanocomposites are suitable for combining MRI detection and photothermal ablation enhanced by applying an external magnetic field.

RESULTS AND DISCUSSION

Filling and Characterization of CNTs with Iron Oxide and/or Cobalt-Based NPs through a Two-Step Process. The CNTs were

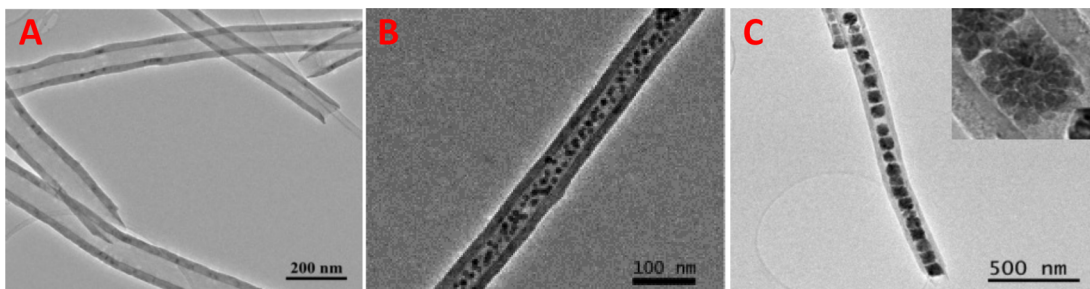


Figure 1. Representative TEM micrographs of pristine MWCNTs (A), $\text{Fe}_{3-x}\text{O}_4$ NPs (B), and CoO NPs (C) inside CNT channels.

filled with magnetic NPs in a high-yield, two-step process. Iron oxide NPs or cobalt-based NPs were first *in situ* synthesized, inside the empty space of the nanotubes, by migration of the precursors in solution. Then a second filling step was performed only with the CNTs filled with iron oxide NPs by inducing the thermal decomposition of either the iron or cobalt precursor. The pristine CNTs display a medium specific surface area of $45 \text{ m}^2 \cdot \text{g}^{-1}$ and exhibit straight and open-ended channels with an average inner diameter around 60 nm and in the range between 40 and 80 nm according to the TEM analysis (Figure 1A). The CNTs were pretreated at 900°C for 4 h under argon flow in order to remove the oxygenated functional groups on their surface before performing the filling. Such treatment is necessary to favor the synthesis of NPs inside CNTs.^{26,27}

TEM micrographs in Figure 1B and Figure S1A (Supporting Information) show that after the first synthesis step involving the decomposition of the iron stearate precursor inside CNTs, $\text{Fe}_{3-x}\text{O}_4$ NPs are cast inside the CNT channels and are rather spherical and homogeneous in size. The average size determined by the statistical analysis of more than 300 NPs is $12.5 \pm 2.4 \text{ nm}$ (Figure S1A, Supporting Information). Some NPs are also formed outside the CNTs, and it is worth noting that the mean size of NPs formed outside the CNTs is $9.8 \pm 1.7 \text{ nm}$, confirming that specific conditions of temperature and pressure inside the CNTs channel (particularly the pressure) were present during the metal oxide NPs synthesis favoring grain growth. The X-ray diffraction (XRD) pattern (Figure S2, Supporting Information) displays the characteristic peaks of a spinel iron oxide phase, and the slight peak at 44.8° is ascribed to the CNTs. The calculated lattice parameter of the spinel phase is $a = 8.394 \text{ \AA}$, and it is close to that of bulk magnetite ($a = 8.396 \text{ \AA}$, JCPDS file 19-0629). One may notice that NPs with similar size synthesized without CNTs have a lattice parameter of $a = 8.381 \text{ \AA}$, intermediate between those of magnetite and its oxidized form, maghemite ($a = 8.346 \text{ \AA}$, JCPDS file 39-1346), confirming that CNTs limit the oxidation of $\text{Fe}_{3-x}\text{O}_4$ NPs.

When the synthesis was performed with the cobalt precursor (Figure 1C and Figure S1B, Supporting

Information), big particles with a dimension tuned by the size of the CNTs channel were observed. TEM images at higher magnification show that they consist of clusters of small NPs (inset in Figure 1C and Figure S1B, Supporting Information). With cobalt stearate, an aggregation process of small nanocrystals into bigger particles was thus observed in CNTs. Such aggregation is often mediated by ligands during solvothermal treatment³⁹ and should be favored by the special pressure and temperature conditions inside CNTs. The XRD pattern (Figure S2, Supporting Information) indicates the presence of two cobalt-based phases: a Co metallic phase (hexagonal structure JCPDS file 89-4308) and a CoO phase (fcc structure (JCPDS file 70-2856) confirming that CNTs limited the oxidation of cobalt. The presence of these two phases was also proved by EELS-STEM analysis (data not shown).

TGA measurements showed a filling yield in the range of 8–10 wt % highly dependent on the washing step when iron stearate was used as precursor. Indeed TEM measurements have been done before and after the purification step: the latter is aimed at removing free NPs and reaction byproducts, and we have noticed that the filling of CNTs was higher before the purification step (Figure S3, Supporting Information). The filling yield was up to 25 wt % when Co stearate was used. The higher filling density of CNTs with cobalt-based NPs is mainly explained by the morphology and the size of cobalt particles. Indeed, the cobalt-based particles have a size similar to the diameter of CNTs and so they are better blocked into the channel. By contrast, iron oxide NPs display a size smaller than the diameter of the CNTs so that they can move easily inside channels and escape. To increase the filling yield and to obtain easily manipulable magnetic CNTs, a second filling step was performed (Scheme 1) only with CNTs filled with iron oxide NPs by inducing the thermal decomposition in presence of the reaction media of either the cobalt or iron stearate precursor. The main objective of this process was to try to block NPs inside the channel of CNTs. It was not possible to increase the filling rate of CNTs with CoO/Co NPs because their large size with respect to the inner diameter of CNTs would not allow introduction of additional precursor. Thus, $\text{Fe}_{3-x}\text{O}_4@\text{CNTs}$ were dispersed again in

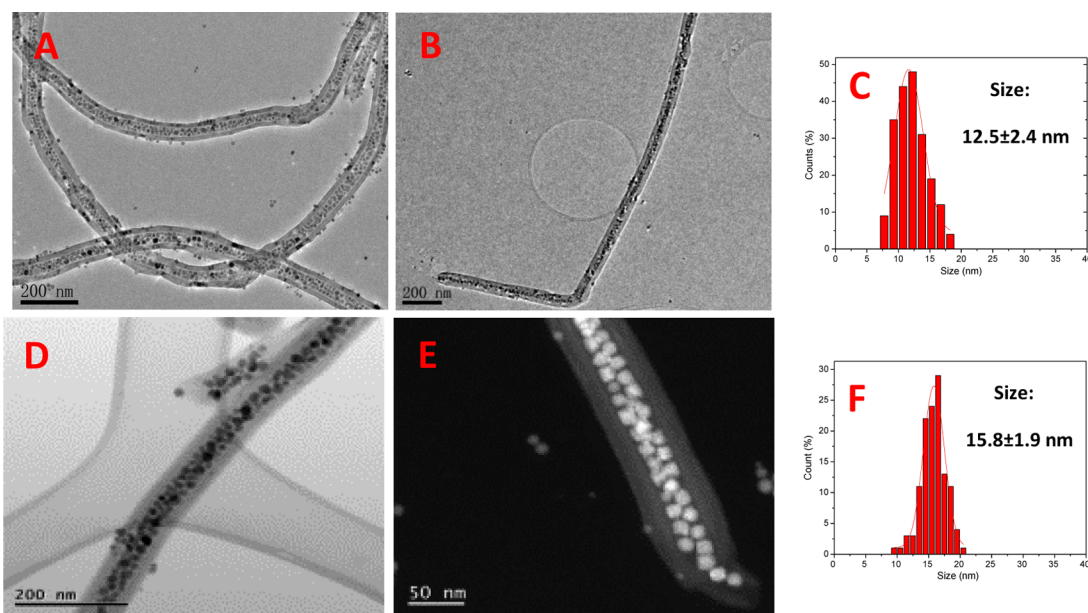


Figure 2. Representative TEM micrographs of $\text{Fe}_{3-x}\text{O}_4/\text{Fe}_{3-x}\text{O}_4$ NPs (A) and $\text{Fe}_{3-x}\text{O}_4/\text{CoO}$ NPs inside CNTs (B). Size distribution of $\text{Fe}_{3-x}\text{O}_4/\text{Fe}_{3-x}\text{O}_4$ NPs inside the CNTs (C). Bright-field (D) and dark-field (E) STEM images of $\text{Fe}_{3-x}\text{O}_4/\text{CoO}$ inside CNTs. Size distribution of $\text{Fe}_{3-x}\text{O}_4/\text{CoO}$ NPs inside CNTs (F).

the octadecene suspension in the presence of either iron stearate or cobalt stearate precursor, and a second thermal decomposition step was performed.

When iron stearate was used, as can be seen in Figure 2A and Figure S4A (Supporting Information), the filling rate with $\text{Fe}_{3-x}\text{O}_4$ NPs was increased and TGA experiments showed a weight gain in the range 15–20%. The iron oxide NPs density inside the channel was thus slightly higher, and their size and shape did not change. An average diameter close to 12.5 nm is measured from TEM images (Figure 2C). By contrast, when cobalt stearate was used, we obtained a larger weight gain (Figure 2B and Figure S4B, Supporting Information), up to 50% from TGA, but one may take into account a contribution of the oxidation of cobalt-based NPs in this weight gain. The chemical analysis showed an iron to cobalt weight ratio of 7 confirming the filling of $\text{Fe}_{3-x}\text{O}_4@\text{CNTs}$ with cobalt. HRTEM images (Figure S4C, Supporting Information) show that NPs are well crystallized. Bright-field (Figure 2D) and dark-field (Figure 2E) STEM images confirmed that the density of NPs inside the channel was very high, and some cube-shaped particles were also observed. The average NP's size is close to 16 nm (Figure 2F) when the average iron oxide NPs size before this step was 12.5 nm. The fact that no characteristic cobalt-based particles were visible (Figure 1C) and that only an increase of the iron oxide based NPs diameter was noticed, strongly suggests the deposition of Co_{1-x}O onto iron oxide NPs.

XRD patterns displayed the characteristic XRD peaks of iron oxide and/or cobalt-based phases (Figure S5, Supporting Information). In the case of $\text{Fe}_{3-x}\text{O}_4/\text{Fe}_{3-x}\text{O}_4@\text{CNTs}$, all peaks match with a spinel iron oxide phase, while with $\text{Fe}_{3-x}\text{O}_4/\text{CoO}@$ CNTs, the

peak at 36.6° and the enlargement of the peaks at 42.5° may be attributed to the presence of CoO. Indeed, no Co metallic phase was identified in $\text{Fe}_{3-x}\text{O}_4/\text{CoO}@$ CNTs.

In order to reveal the distribution of the newly formed Co_{1-x}O phase with regard to the initial $\text{Fe}_{3-x}\text{O}_4$ NPs, energy-filtered TEM (EFTEM) analyses have been performed on the filled CNTs by the two-step process. EFTEM is a powerful analytic technique which can elucidate if, after the second filling with Co stearate, new Co-based NPs are formed or the CoO phase is deposited around the preexisting Fe_3O_4 NP by heterogeneous growth, thus leading to "core–shell" structures.⁴⁰ First, an EELS spectrum was acquired (Figure S6, Supporting Information) displaying two peaks, which correspond to Fe and Co elements. Elemental maps acquired based on the EELS spectrum characteristics (see Figure 3) show a homogeneous distribution of Fe and Co along all the CNTs. As can be observed in Figure 3B, Fe is distributed in well-defined areas proving the presence of $\text{Fe}_{3-x}\text{O}_4$ NPs synthesized during the first step. The Co map (Figure 3C) shows a relatively low signal which is due to the Co peak position in the EELS spectrum. However, it is clear that Co is homogeneously distributed around the preexisting Fe_3O_4 NPs. This aspect is better highlighted by the RGB composite of the Fe and Co maps presented in Figure 3D. As the low signal-to-noise ratio obtained for the Co elemental map does not allow us to precisely indicate the position of the Co_{1-x}O phase with respect to the $\text{Fe}_{3-x}\text{O}_4$ NPs, we have performed on the same system a STEM-EELS analysis. By scanning on single nanoparticle from one side to another and simultaneously extracting the EELS data the exact position of each element is extracted. The results show that Co_{1-x}O can either

form a homogeneous shell around the $\text{Fe}_{3-x}\text{O}_4$ NPs leading to a core–shell structure (Figure 4a) or can create patches, leading to an inhomogeneous coverage around the $\text{Fe}_{3-x}\text{O}_4$ NPs (Figure 4b).

Magnetic measurements were then performed to evaluate the composition of core–shell NPs. Indeed, if they are constituted of iron oxide NPs coated with CoO ($\text{Fe}_{3-x}\text{O}_4@\text{CoO}$), exchange bias properties should be observed as $\text{Fe}_{3-x}\text{O}_4$ and CoO phases are ferrimagnetic and antiferromagnetic, respectively. Hysteresis loop measurements (Figure 5a) displayed at first their superparamagnetic behavior at 400 K. Exchange coupling at the FM/AFM interface of $\text{Fe}_{3-x}\text{O}_4/\text{CoO}@\text{CNTs}$ was investigated by field cooling (FC) measurements (magnetic measurements after cooling down magnetic CNTs under an applied magnetic field). In Figure 5b, only a slight horizontal shift of the FC hysteresis loop can be observed, with respect to the ZFC hysteresis loop of $\text{Fe}_{3-x}\text{O}_4/\text{CoO}@\text{CNTs}$, indicating a weak exchange bias ($H_E = 355$ Oe). Indeed, very large exchange fields (higher than 10000 Oe) are generally observed in $\text{Fe}_{3-x}\text{O}_4@\text{CoO}$ core–shell NPs.⁴⁰ Hence, we can conclude that there is not a large population of uncompensated spins in a ferrimagnetic (FM)– $\text{Fe}_{3-x}\text{O}_4/$

antiferromagnetic (AFM)–CoO interface. However, a large coercivity H_c ($H_c = 8250$ Oe) of $\text{Fe}_{3-x}\text{O}_4/\text{CoO}@\text{CNTs}$ was observed in comparison to the small value of H_E ,⁴¹ and furthermore, it was substantially larger than that of $\text{Fe}_{3-x}\text{O}_4/\text{Fe}_{3-x}\text{O}_4@\text{CNTs}$ ($H_c = 330$ Oe).

Considering all these results and our recent results on the magnetic properties of core–shell $\text{Fe}_{3-x}\text{O}_4@\text{CoO}$ NPs displaying different CoO shell thicknesses (to be published), this drastic enhancement of coercive field can only be explained by the formation of cobalt ferrite (which is known to display a large magnetocrystalline anisotropy) inside CNTs either as a fine layer at the surface of iron oxide NPs or as cobalt ferrite NPs. The NPs' size increase and TEM analyses suggest the formation of a fine layer of cobalt ferrite at the iron oxide–NP surface. This can be due either to the simultaneous decomposition of cobalt stearate and residual iron stearate (as the products are not purified before the second filling step) or to the Co diffusion into the first surface atomic layer of $\text{Fe}_{3-x}\text{O}_4$ NPs.^{42,43} The identification of CoO by XRD suggests also that a fine layer of CoO is present and thus that some $\text{Fe}_{3-x}\text{O}_4@\text{Co}_x\text{Fe}_{2-y}\text{O}_4@\text{CoO}$ core–shell NPs were formed in the samples.

The slightly smaller saturation magnetization at 5 K of $\text{Fe}_{3-x}\text{O}_4/\text{CoO}@\text{CNTs}$ (75 emu/g), in comparison with that of $\text{Fe}_{3-x}\text{O}_4/\text{Fe}_{3-x}\text{O}_4@\text{CNTs}$ (81 emu/g), could be attributed to the nonmagnetic contribution of the antiferromagnetic CoO phase. One may notice that the saturation magnetization value of $\text{Fe}_{3-x}\text{O}_4/\text{Fe}_{3-x}\text{O}_4@\text{CNTs}$ is higher than that of NPs of similar sizes which were synthesized in the absence of CNTs (~60 emu/g).^{44,45} Magnetization measurements as a function of temperature are also shown in Figure 5c. The ZFC maximum, often attributed to the blocking temperature T_B , is at 305 and 119 K for $\text{Fe}_{3-x}\text{O}_4/\text{CoO}@\text{CNTs}$ and $\text{Fe}_{3-x}\text{O}_4/\text{Fe}_{3-x}\text{O}_4@\text{CNTs}$, respectively. The ZFC curve of $\text{Fe}_{3-x}\text{O}_4/\text{Fe}_{3-x}\text{O}_4@\text{CNTs}$ is quite broad, suggesting a distribution of blocking temperatures and/or of the distribution of strength of dipolar interactions as long as they induce a shift of the blocking temperature. The high ZFC maximum for $\text{Fe}_{3-x}\text{O}_4/\text{CoO}@\text{CNTs}$ is in agreement with the presence

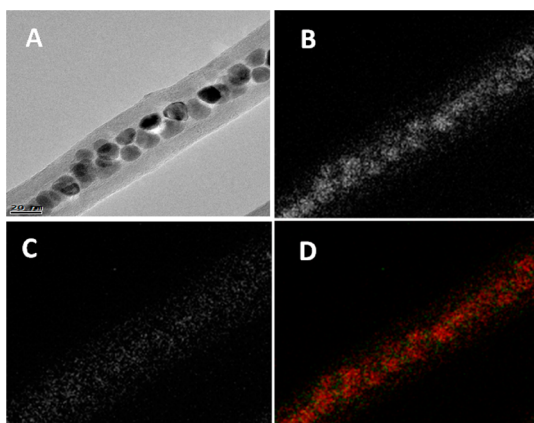


Figure 3. (A) TEM image of $\text{Fe}_{3-x}\text{O}_4/\text{CoO}@\text{CNTs}$. (B) Elemental map of Fe extracted from region presented in 3A. (C) Elemental map of Co extracted from region presented in 3A. (D) Color composite of the Fe (in red) and Co (in green) maps.

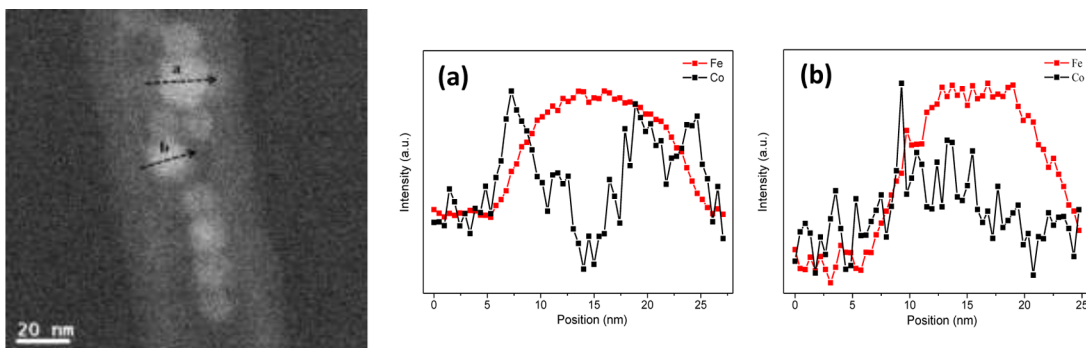


Figure 4. (Left) STEM dark-field image of $\text{Fe}_{3-x}\text{O}_4/\text{CoO}@\text{NPs}$ inside CNTs showing the position of NPs (a and b) along line a and b: corresponding Fe and Co atoms amounts (%) as a function of the NP section.

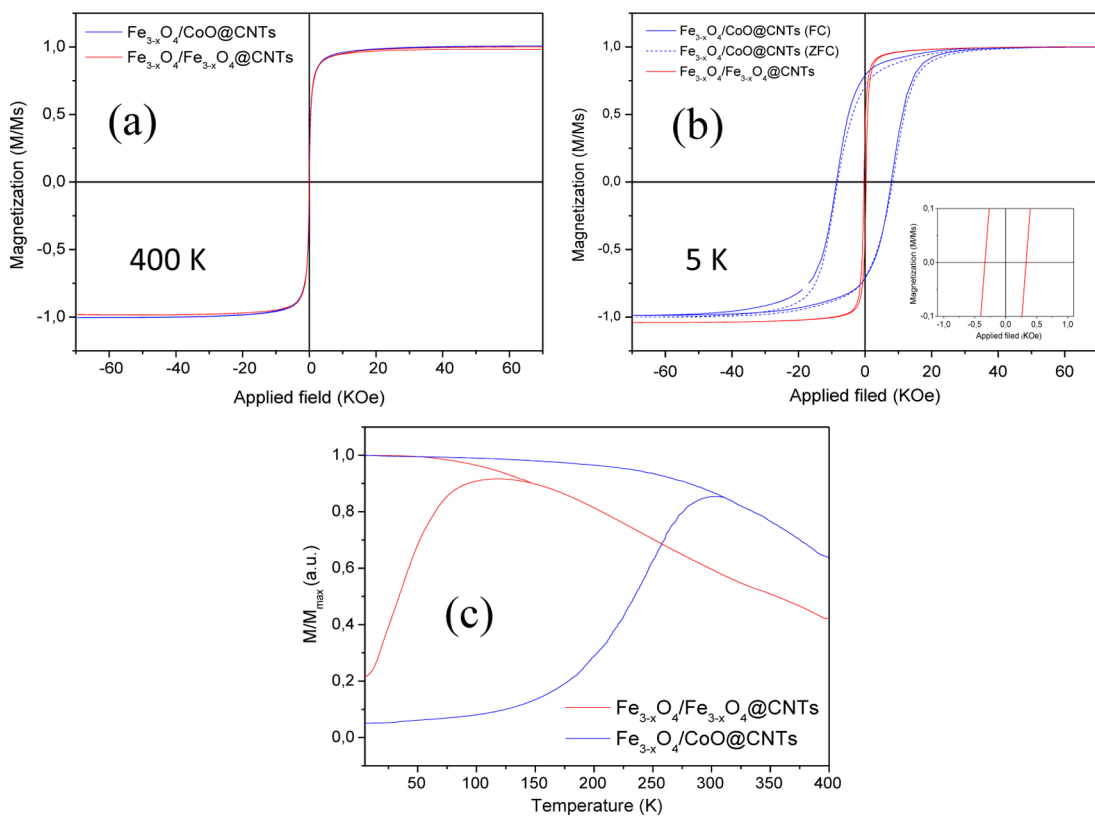


Figure 5. (a) Magnetization curves of $\text{Fe}_{3-x}\text{O}_4/\text{CoO}@\text{CNTs}$ and $\text{Fe}_{3-x}\text{O}_4/\text{Fe}_{3-x}\text{O}_4@\text{CNTs}$ at 400 K and (b) before (ZFC) and after (FC) cooling from 400 to 5 K under magnetic field and $\text{Fe}_{3-x}\text{O}_4/\text{Fe}_{3-x}\text{O}_4@\text{CNTs}$ at 5 K. (Inset: enlargement of curve of $\text{Fe}_{3-x}\text{O}_4/\text{Fe}_{3-x}\text{O}_4@\text{CNTs}$.) (c) Magnetization versus temperature (ZFC (blue) and FC (red) curves) of $\text{Fe}_{3-x}\text{O}_4/\text{CoO}@\text{CNTs}$ and $\text{Fe}_{3-x}\text{O}_4/\text{Fe}_{3-x}\text{O}_4@\text{CNTs}$.

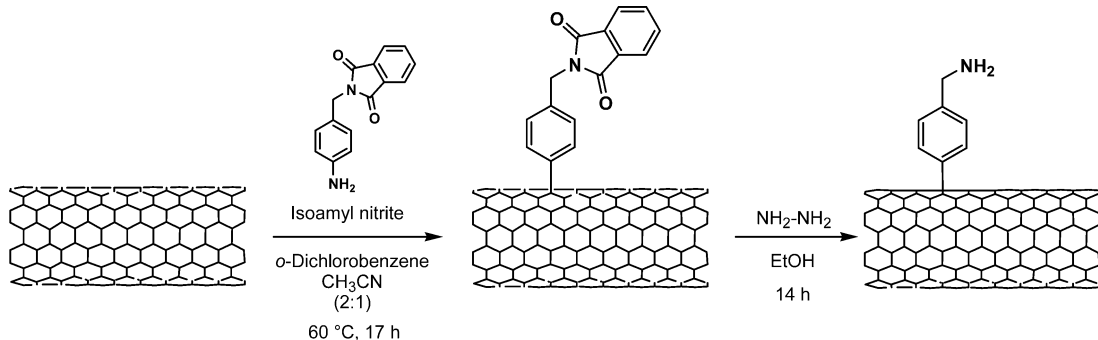


Figure 6. Functionalization of CNTs by arylation and subsequent Pht deprotection. For simplicity, only one functional group per tube is shown.

of the anisotropic cobalt ferrite phase.⁴⁶ Thus, these filled CNTs display suitable magnetic properties to be manipulated by an external field. This was further confirmed by applying an external magnetic field on a suspension of magnetic CNTs (Figure S7, Supporting Information). After 10 min, the sample was attracted toward the wall of the vial.

Functionalization of Magnetic CNTs. As the CNTs have been heat-treated to remove oxygenated groups prior to the formation of the NPs, they are not dispersible in water (Figure S8, Supporting Information). Hence, we functionalized the filled CNTs by arylation to introduce amino groups on the nanotube sidewall. The reaction

was first tested on the nonfilled MWCNTs (Figure 6). For this purpose, the CNTs were reacted with diazonium salts generated *in situ* by reaction of a Pht-protected 4-(aminomethyl)phenylamine derivative and isoamyl nitrite.^{47,48} The Pht group was then removed in the presence of hydrazine.

UV-vis spectroscopy was used to assess the amount of amine functions by the Kaiser test.^{49,50} The level of functionalization was 67 μmol NH₂ per gram of CNTs. As the diameter and the number of layers are high, the loading values are relatively low compared to the functionalization of thinner MWCNTs.⁴⁸ However, the number of amino groups was sufficient to impart water

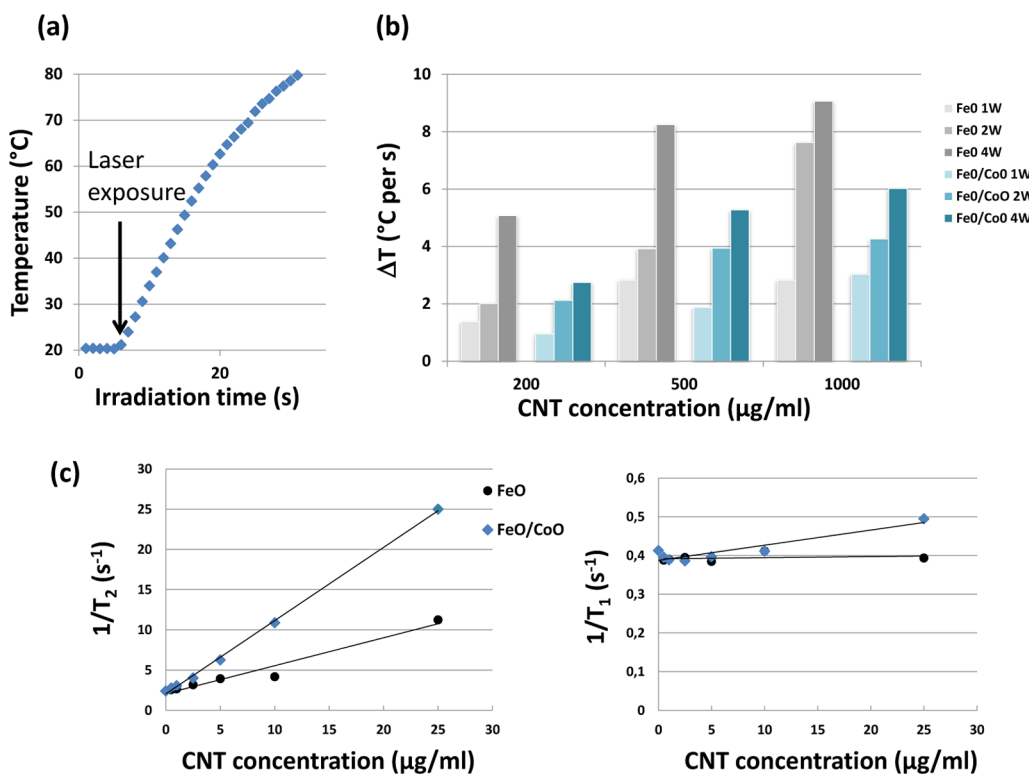


Figure 7. (a) Example of heating profile in a 50 μ L water suspension of $\text{Fe}_{3-x}\text{O}_4/\text{CoO}$ @CNTs (200 $\mu\text{g}/\text{mL}$) exposed to a 808 nm laser at a fluence of 4 W/cm^2 . (b) Temperature increase per second in a 50 μL suspension of $\text{Fe}_{3-x}\text{O}_4/\text{CoO}$ @CNTs (FeO/CoO) and $\text{Fe}_{3-x}\text{O}_4/\text{Fe}_{3-x}\text{O}_4$ @CNTs (FeO) at different CNT concentrations when exposed to a NIR laser at a fluence of 1, 2, or 4 W/cm^2 . (c) MRI contrast properties of $\text{Fe}_{3-x}\text{O}_4/\text{CoO}$ @CNTs and $\text{Fe}_{3-x}\text{O}_4/\text{Fe}_{3-x}\text{O}_4$ @CNTs: the longitudinal and transverse relaxation rates of proton magnetization, $1/T_1$ and $1/T_2$, measured at 4.7 T (200 MHz) show a linear dependence with CNT concentration. The slope of the linear dependence represents the relaxivity r_1 and r_2 .

dispersibility. The functionalized CNTs were characterized by TGA under inert atmosphere (Figure S9, Supporting Information). As expected, the pristine CNTs were stable up to high temperature, and no significant weight loss was observed. In the case of Pht-functionalized CNTs, the weight loss observed corresponds to the amount of functional groups introduced on the nanotube surface that are thermally labile. The main weight loss takes place at 450 °C, while the Pht-protected 4-(aminomethyl)phenylamine derivative is thermally degraded at a lower temperature (350 °C) (data not shown). These results confirm that covalent functionalization of the CNTs occurred. The NH_2 -functionalized CNTs were used as controls for *in vitro* cell experiments (*vide infra*). The arylation reaction was then tested on the filled CNTs to increase their water dispersibility. The level of functionalization was 16 and 14 μmol of NH_2 per gram of $\text{Fe}_{3-x}\text{O}_4/\text{CoO}$ @CNTs and $\text{Fe}_{3-x}\text{O}_4/\text{Fe}_{3-x}\text{O}_4$ @CNTs, respectively. The presence of amino groups allowed dispersal of the filled CNTs in water (Figure S8, Supporting Information). Compared to the functionalization of pristine CNTs, the loading values are inferior as the relative amount of amino groups per gram of CNT material is lower due to the presence of NPs inside the nanotubes. The water-dispersible filled CNTs were observed by TEM to check that the functionalization process did not induce any

release of NPs. In addition, diameter and length of the tubes were not affected by the functionalization.

Biomedical Potential of Functionalized Magnetic CNTs. In order to demonstrate the biomedical potential of the water-dispersible magnetic CNTs, we first evaluated their properties as heat mediators for photothermal ablation and as contrast agent for MRI, which are key features to combine monitoring and efficient treatment. We evaluated the heating efficiency of magnetically loaded CNTs in comparison to the nonmagnetic precursor CNTs. A 50 μL water suspension of CNTs (200–1000 $\mu\text{g}/\text{mL}$) was irradiated using a fiber optic laser device operating at an NIR wavelength of 808 nm. Soon after laser irradiation, the nanotube suspension started to heat and attained boiling temperature in less than 1 min (Figure 7a) at a fluence of 4 W/cm^2 . Under the same conditions of laser irradiation, CNTs-free water showed a temperature increase of less than 1°. The nanotube heating capacity was evaluated at different CNT concentrations and radiant exposures (Figure 7b). When normalized to the laser fluence, the specific absorption rate (SAR) of CNTs, expressed in watt per mass of materials, was maximum at 1 W/cm^2 and CNTs concentration of 200 $\mu\text{g}/\text{mL}$ (Table 1). Actually, with higher concentrations of CNTs, the light was strongly absorbed and did not penetrate the whole sample volume, therefore diminishing the overall

TABLE 1. Iron and Cobalt Mass Fraction, Specific Absorption Rate under 808 nm NIR Radiant Exposure of 1 W/cm², and MRI Relaxivities Measured at 4.7 T

	Fe _{3-x} O ₄ /CoO@CNTs (%)	Fe _{3-x} O ₄ /Fe _{3-x} O ₄ @CNTs (%)	CNTs (%)
iron content (in mass)	39.70	6.64	0
cobalt content (in mass)	5.85	0	0
SAR (W/g)			
CNT (200 μ g/mL)	19855	28842	33649
CNT (500 μ g/mL)	15717	23660	21067
CNT (1000 μ g/mL)	12665	11830	14964
relaxivity related to iron concentration (mM)			
r_1 (s ⁻¹ mM ⁻¹)	0.55	2	
r_2 (s ⁻¹ mM ⁻¹)	128	286	
relaxivity related to the concentration of materials			
r_1 (s ⁻¹ (μ g/mL) ⁻¹)	0.004	0.024	
r_2 (s ⁻¹ (μ g/mL) ⁻¹)	0.9	0.34	
r_2/r_1	232	143	

relative heating efficiency. Comparatively, Fe_{3-x}O₄/Fe_{3-x}O₄@CNTs were more efficient heaters than Fe_{3-x}O₄/CoO@CNTs (Table 1). If we assume that the carbon backbone shows better energy transduction in comparison to the magnetic particles, the lower magnetic content and higher carbon amount per gram of materials in Fe_{3-x}O₄/Fe_{3-x}O₄@CNTs could explain their greater SAR. The later explanation is also in line with the slightly higher SAR of precursor nanotubes.

While the encapsulated magnetic materials minimally affect the excellent photothermal properties of CNTs, it confers outstanding contrast properties for MRI detection. In order to determine their MRI relaxivities, CNTs were dispersed in agarose gels at seven different concentrations (from 0.5–25 μ g/mL) and imaged on the 4.7T MRI scanner. The spin–lattice (T1) relaxation time as well as the spin–spin (T2) transversal relaxation time were deduced from signal measurement at different repetition and echo times using spin–echo sequences. The relaxation rates, 1/T1 and 1/T2, respectively, vary linearly with CNT concentrations (Figure 7c), allowing us to define the concentration-independent relaxivity r_1 and r_2 related to iron or to CNT concentrations (Table 1). It is worth noting that the very high values of the ratio r_2/r_1 place both types of magnetic carbon nanotubes as excellent T2 contrast agents. The confinement of magnetic nanoparticles into the unidirectional hollow architecture of CNTs is favorable, on one hand, to the reduction of longitudinal relaxivity due to diminished access of water proton to the magnetic centers and, on the other hand, to the enhancement of transverse relaxivity which arises from assembling nanoparticles in a small confined volume.^{51–53} In addition, one dimensional cooperative assembly of iron oxide NPs was shown to enhance spin–spin relaxation of water molecules.⁵⁴ Here, the *in situ* growth of magnetic NPs, which mostly takes place into the cylindrical cavity of the tube, allows enhancement of the magnetization and subsequently increases the transverse relaxivity in comparison to

previously reported CNTs decorated with magnetic particles on their outer layer.^{22,55–57} Interestingly, related to CNT concentration, Fe_{3-x}O₄/CoO@CNTs are more efficient T₂ contrast agents than Fe_{3-x}O₄/Fe_{3-x}O₄@CNTs in line with their higher magnetic content (Table 1). Moreover, the greater confinement of nanoparticles into Fe_{3-x}O₄/CoO@CNTs results in lower r_1 and higher r_2 in comparison to Fe_{3-x}O₄/Fe_{3-x}O₄@CNTs. On the basis of iron concentration, Fe_{3-x}O₄/Fe_{3-x}O₄@CNTs show, however, much higher r_2 values than commercial iron oxide NPs and comparable values with polymer-embedded clusters of nanoparticles, 3D iron oxide cooperative nanoflowers, or 1D iron oxide nanoworms.^{58–60} Combined with the water dispersibility and the possibility to further functionalize the external layer of nanotubes, our system provides the first example of highly anisotropic magnetic structures with micrometric length and large aspect ratio (>20) that are evaluated for MRI.

Encouraged by the high performance of CNTs for MRI and photothermal ablation, the next step was to assess their behavior on contact with cells. The magnetic CNTs were incubated with SKOV3 ovarian cancer cells. In order to assess the innocuousness of Fe_{3-x}O₄/CoO@CNTs and Fe_{3-x}O₄/Fe_{3-x}O₄@CNTs, cells were incubated with those nanohybrids for 48 h up to a concentration of 50 μ g/mL. The cell aspect (Figure 8a) and metabolic activity measured by the Alamar Blue test at 24 and 48 h after treatment (Figure 8b) were identical to those of the control nonexposed cells regardless of the concentration of CNTs.

We then evaluated how magnetic fields can modulate the nanotube/cell interactions. As illustrated in Figure 9, the cellular uptake of CNTs consists of two phases: the early interaction with the plasma membrane which is clearly seen in SEM pictures of Figure 9a (30 min incubation) followed by internalization of CNTs from the plasma membrane into membrane-bound intracellular vesicles (90 min incubation, Figure 9b,c). Remarkably, the application of a magnetic field parallel or perpendicular to the cell monolayer during the

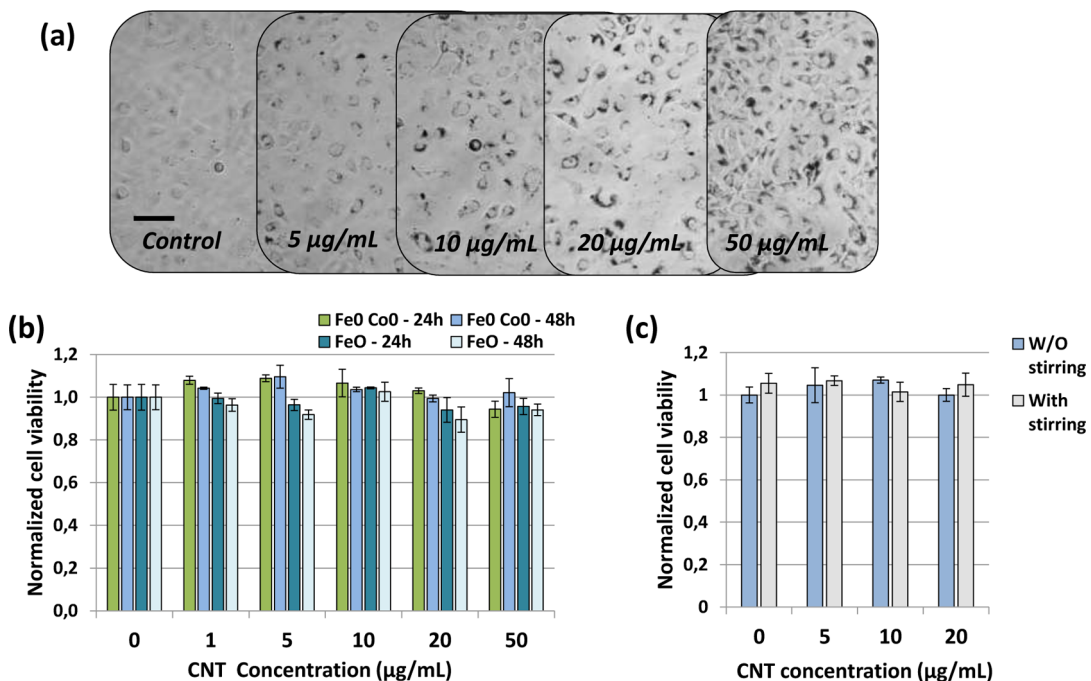


Figure 8. (a) Optical micrographs of SKOV3 cells after 24 h incubation with $\text{Fe}_{3-x}\text{O}_4/\text{CoO}$ @CNTs at different concentrations. Scale bar = 50 μm . (b) Metabolic activity of SKOV3 ovarian carcinoma cells incubated for 24 h with $\text{Fe}_{3-x}\text{O}_4/\text{CoO}$ @CNTs and $\text{Fe}_{3-x}\text{O}_4/\text{Fe}_{3-x}\text{O}_4$ @CNTs at concentrations of 0, 1, 5, 10, 20, and 50 $\mu\text{g/mL}$ normalized to that of control nonexposed cells. Metabolic activity was measured at 24 and 48 h after the start of incubation. (c) Metabolic activity of SKOV3 ovarian carcinoma cells incubated for 30 min with $\text{Fe}_{3-x}\text{O}_4/\text{CoO}$ @CNTs and exposed (or nonexposed) to 30 min magnetic stirring at 1 Hz. Metabolic activity was measured 24 h after treatment.

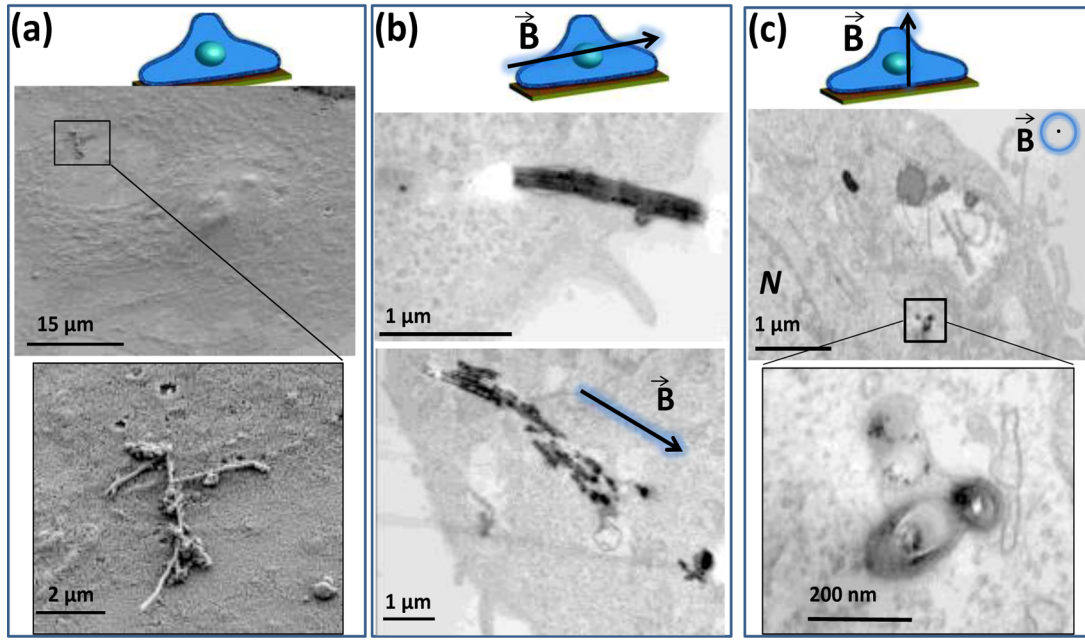


Figure 9. Magnetic control of CNT positioning to direct oriented cell uptake. (a) SKOV3 tumor cells were incubated with $\text{Fe}_{3-x}\text{O}_4/\text{CoO}$ @CNTs (5 $\mu\text{g/mL}$) for 30 min without magnetic field. SEM observation reveals the early adsorption of CNTs on the plasma membrane. (b, c) Alternatively, the incubation with CNTs was carried out in presence of a magnetic field either parallel (b) or perpendicular (c) to the cell monolayer, for 90 min. Cells were fixed in the presence of the field and processed for TEM (TEM slice parallel to the cell layer). Electron micrographs show the CNTs within intracellular membrane compartments that are aligned in the direction of the applied field, either parallel (b) or perpendicular to the cell layer (c). CNTs penetrate the cell perpendicularly to the cell layer in presence of a perpendicular field. Note the presence of membranes all around internalized CNTs.

uptake process has the potential to direct nanotube orientation and further enhance cell internalization. As

seen in Figure 9b, the vesicles containing CNTs attract each other and form bundles oriented along the field

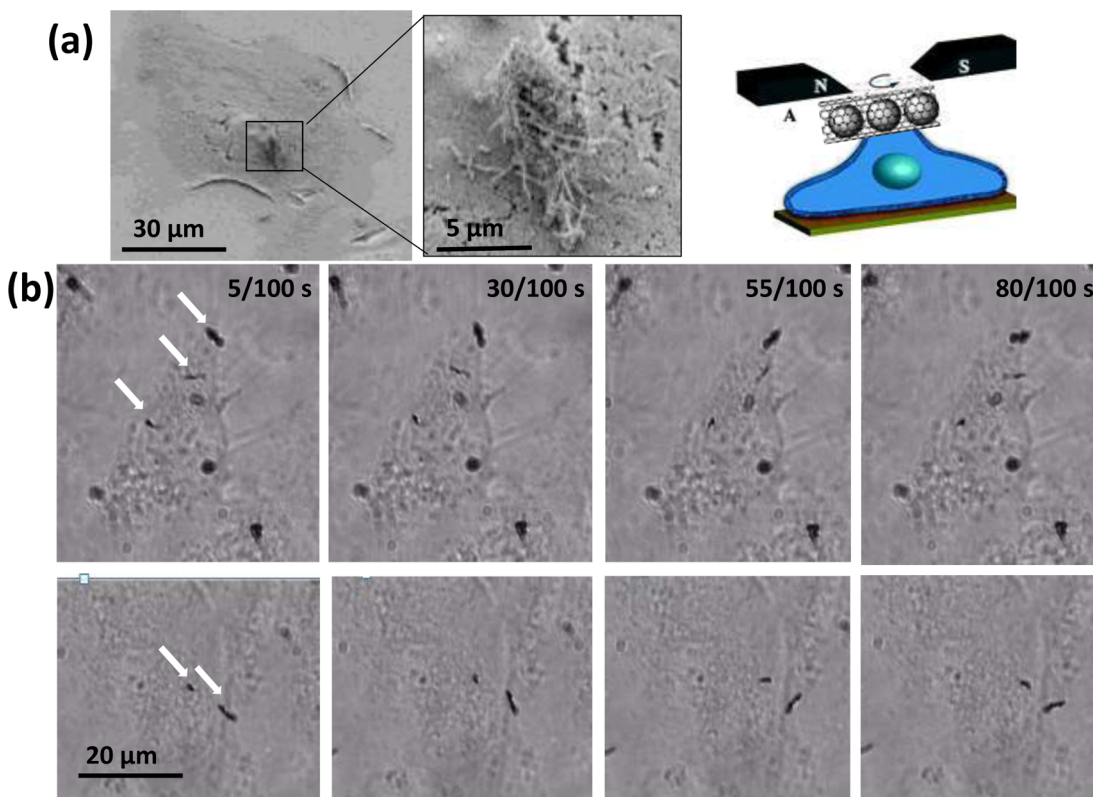


Figure 10. Magnetic stirring of CNTs on tumor cells. SKOV3 tumor cells were incubated with $\text{Fe}_{3-x}\text{O}_4/\text{CoO}$ @CNTs (5 $\mu\text{g}/\text{mL}$) for 30 min. (a) SEM micrographs shows the nanotubes at the surface of the cells. (b) Cells were then submitted to a rotating magnetic field at a frequency of 1 Hz and videotaped. Pictures show the same cells at time intervals of 25/100 s. White arrows point out rotating CNTs on the cell surface.

direction parallel to the cell layer. Conversely, when the magnetic field is applied perpendicularly to the cell layer, the CNTs stand perpendicularly as well and we observe transverse slices of the carbon backbone with membrane around and NPs inside (Figure 9c).

The magnetic responsivity of CNTs also allows their dynamical activation on the cell membrane. After short incubation with cells (30 min), the CNTs were shown to rotate on the cell membrane when exposed to a rotating magnetic field in the plane of the monolayer. Indeed time-lapse videomicroscopy of cells shows several black bundles rotating at the 1 Hz frequency of the applied field (Figure 10). Note that the phase lag of CNT orientation with respect to the applied field could vary depending on CNT anchorage on the cell membrane. Remarkably, no deleterious effect was observed on cells even after 30 min of magnetostirring: the cells kept their initial shape and aspect and were still able to divide following magnetic stimulation. Their metabolic activity assessed 24 h after magnetic stirring was identical for treated and nontreated cells regardless of CNT concentrations (Figure 8c). These observations contrast with previous experiments showing cell lysis induced by the rotation of large bundles of MWCNTs on the surface of cells.⁶¹ In the latter study, the magnetic response of nanotubes relied on the iron/nickel catalyst impurities that they

contained and the rotating large aggregates of CNTs could impact the integrity of cell membrane. In our study, CNT functionalization, high water dispersibility, controlled magnetic content, and magnetically directed orientation allows a spatial and temporal control of their interaction with cells without affecting cell viability.

In addition, cellular uptake in single cells could be quantified thanks to the magnetic properties of the CNTs. As illustrated in Figure 11a, a labeled cell can be attracted by a magnet and its individual magneto-phoretic mobility is proportional to the mass of CNT uptake. Indeed, using a single-cell magnetophoresis set up, the magnetic force on cells (proportional to the calibrated magnetic field gradient and to the magnetization of the cell) simply balances the viscous force (proportional to the cell diameter, cell velocity, and viscosity of the carrier fluid) when the permanent regime is attained. Hence, the cell-by-cell measurements of velocity and diameter provide the whole distribution of magnetic nanotube uptake, knowing the magnetization of nanotubes. In comparison to cells incubated with $\text{Fe}_{3-x}\text{O}_4/\text{Fe}_{3-x}\text{O}_4$ @CNTs, the cell labeled with $\text{Fe}_{3-x}\text{O}_4/\text{CoO}$ @CNTs showed more than 3-fold higher magnetic mobility, which is consistent with the higher iron content and magnetization of those nanohybrids (Figure 11b). When expressed as

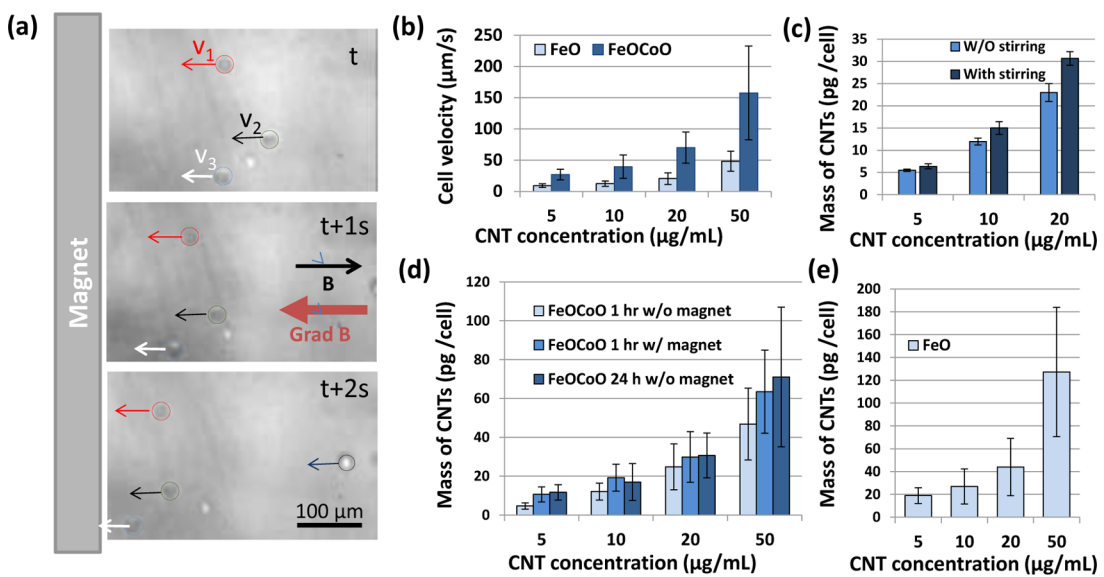


Figure 11. Magnetophoretic mobility of CNT-labeled cells allows quantifying CNT uptake. SKOV3 cells were incubated with $\text{Fe}_{3-x}\text{O}_4/\text{CoO@CNTs}$ (FeOCoO) or $\text{Fe}_{3-x}\text{O}_4/\text{Fe}_{3-x}\text{O}_4@\text{CNTs}$ (FeO) at concentrations of 5–50 $\mu\text{g/mL}$ for 30 min to 24 h. The influence of a magnet which both orients and attracts CNTs perpendicularly to the cell layer was tested for the 1 h condition. The influence of magnetic stirring on cell uptake was also tested. The labeled cells were then trypsinized and put in suspension in the presence of a calibrated magnetic field gradient that makes cells moving to the magnet. In a permanent regime (constant cell velocity) (see v_1 , v_2 , v_3 as examples of cell velocity in (a)), the viscous force experienced by the moving cells directly balance the magnetic force. Thus, the measurement of cell velocity (b) allows quantifying magnetic force on each cell and corresponding CNT uptake (c–e). Here the cell velocity (b) and the mass of CNTs per cell (c–e) were averaged over 40 individual cells. Bars represent standard deviation of the distribution of velocity or CNT mass over the cell population. (b) Magnetophoretic velocity of cells incubated for 24 h with FeOCoO or FeO . (c) Mass of CNTs in cells (pg per cell) incubated with FeOCoO for 30 min and submitted or not to 30 min magnetic stirring. Magnetic stirring tends to increase cellular uptake. (d) Mass of CNTs in cells (pg per cell) incubated with FeOCoO for 1 h with or without magnet or for 24 h without magnet. (e) Mass of CNTs in cells incubated with FeO for 24 h without magnet.

mass of nanotube, however, cellular uptake was higher for $\text{Fe}_{3-x}\text{O}_4/\text{Fe}_{3-x}\text{O}_4@\text{CNTs}$ (Figure 11d). For both nanohybrids, the cell load increased with increasing CNT concentrations during incubation. We also investigated the influence on cell uptake of 30 min magnetic stirring after 30 min incubation with $\text{Fe}_{3-x}\text{O}_4/\text{CoO@CNTs}$ (Figure 11c). Interestingly, CNT uptake tends to be increased by magnetic stirring. To assess the effect of a perpendicular magnetic force on cell uptake (the so-called magnetofection effect), cells were also incubated for 1 h with or without a magnet placed under the culture flask (Figure 11d). Interestingly, the presence of the magnet significantly increased cellular uptake, which can be explained by an enhanced accumulation of $\text{Fe}_{3-x}\text{O}_4/\text{CoO@CNTs}$ on the cell membrane due to the magnetic driving force and putatively to its normal orientation with respect to the cell basement. Further increase of incubation time up to 24 h (without the magnet) did not significantly increase CNT uptake in comparison to the 1 h magnet condition. Therefore, we can conclude that magnetically assisted targeting of cancer cells by $\text{Fe}_{3-x}\text{O}_4/\text{CoO@CNTs}$ allows fast and efficient uptake that could reach 64 pg CNTs/cell in 1 h while preserving cell viability.

Finally, the efficacy of $\text{Fe}_{3-x}\text{O}_4/\text{CoO@CNTs}$ for photothermal cytology was evaluated. Adherent cells were treated for 200 or 500 s with NIR irradiation

(4 W/cm²) soon after incubation with CNTs and rinsing (1 h with magnet or 24 h without magnet). Cell viability was quantified 24 h after NIR treatment which is a sufficient delay to observe apoptosis or necrosis (Figure 12). The laser had no deleterious effect on control nonlabeled cells. In contrast, we observed a dose-dependent NIR light-induced toxicity on labeled cells, which increased with increasing cellular load of CNTs and with the time of laser exposure. Remarkably, 80% cell death was attained with the 1 h magnet condition (50 $\mu\text{g/mL}$, 64 pg CNTs/cell). It is worthy of note that despite the comparable amount of CNTs in cells after 24 h incubation, NIR toxicity was significantly higher after 1 h incubation with the magnet, regardless of the irradiation time. One hypothesis is that the localization of CNTs near the plasma membrane at short times amplified cell damage due to local heating in comparison with CNTs having intracellular localization at 24 h. Further studies are underway in order to unravel this interesting localization effect. Overall, our data indicate excellent potential of $\text{Fe}_{3-x}\text{O}_4/\text{CoO@CNTs}$ for photothermal ablation. The comparison with other nanotubes is not straightforward since the quantity of CNTs per cell is rarely measured.¹⁹ Here, the magnetic properties of nanotubes uniquely allow for accurate quantification of CNTs uptake by single cells. In addition, we have shown very efficient uptake by tumor cells, which could be enhanced by magnetic targeting

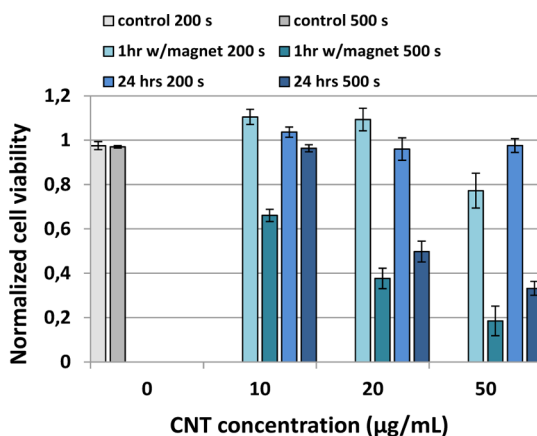


Figure 12. Viability of SKOV3 cells exposed to 808 nm NIR laser at a fluence of 4 W/cm^2 for 200 or 500 s laser for different labeling condition with $\text{Fe}_{3-x}\text{O}_4/\text{CoO@CNTs}$ in comparison to irradiated nonlabeled control cells. The metabolic activity of cells was normalized to that of nonlabeled nonirradiated cells.

and magnetic stirring. Finally, for similar amount of CNTs per cell, the localization of nanotubes appears to play a role on the NIR-induced damage on cells.

Although the magnetic CNTs were not injected *in vivo* in this study, their high heating efficiency and high dispersibility make them suitable for intratumoral injection and precise photothermal ablation of tumors using NIR radiation that can penetrate the tissue more than 1 cm.¹⁹ In this context, we are currently planning a detailed study on the *in vivo* therapeutic potential of these hybrids and on the evaluation of their pharmacokinetic profile. In addition to the photothermal response of NP-loaded CNTs, we also tested the magnetically induced heating when submitted to an alternative magnetic field of 700 kHz and 24 kA/m. However, at CNT concentrations used for photothermal ablation ($<1000 \mu\text{g/mL}$), we did not observe any significant heating under a magnetic field. This is consistent with typical magnetic SAR of the order of 10–1000 W/g of magnetic NPs compared with the huge SAR of CNTs under laser exposure ($>10000 \text{ W/g}$).

EXPERIMENTAL SECTION

Nanohybrid Synthesis. Starting MWCNTs were provided by Pyrograph Products (Cedarville, OH). Their inner diameters are typically between 40 and 80 nm. They were first washed with HNO_3 to remove traces of the residual iron growth catalyst. To remove the maximum number of oxygenated species on their surface they were heated at 900°C under an inert atmosphere for 4 h. The elimination of oxygenated groups at the surface of CNTs has been confirmed by photoelectron spectroscopy (XPS).

Syntheses of metal oxides NPs^{44,45} and MxOy@CNTs ^{26,27} have already been described elsewhere: for the first filling step, CNTs were first dispersed in octadecene under ultrasonication. Iron (or cobalt) stearate was then added, and the solution was heated at 120°C for 12 h to dissolve the reactants, to eliminate the traces of water or impurities, and to favor the diffusion of metal precursor inside CNTs. Then, the mixtures were heated at 318°C (heating rate $5^\circ\text{C}/\text{min}$) under air for 2 h. Finally, the

Thus, NP-loaded CNTs are much more efficient photothermal agents than magnetothermal agents, but their magnetic properties are uniquely exploited both for MRI monitoring and magnetic manipulation. Another concern for *in vivo* applications is the biodegradability of CNTs. The filling of CNTs with nanoparticles provides a unique label to investigate the structural integrity of the carbon backbone during cell processing. A comprehensive study to investigate the long-term behavior of NPs-loaded nanotubes is underway. We confirm here that there is no release of NPs in water or in cell culture incubation medium since no isolated NPs could be seen in different cell compartments. After 6 h of incubation with tumor cells, we mainly observe NPs entrapped into the internalized nanotubes. However, in one cell we could observe the release of NPs from the nanotubes (Figure S10, Supporting Information), suggesting the degradation process can rapidly occur taking place first at the nanotube extremities.

CONCLUSION

Carbon nanotubes filled with magnetic NPs have been successfully obtained with a high filling rate (up to 50 wt %) by an original double-filling process. Despite the removal of oxidizing groups at the surface of CNTs to trigger the synthesis of NPs inside CNTs, we succeeded in functionalizing them by amino groups to ensure good dispersibility in aqueous medium.

The properties of the filled magnetic CNTs as heat mediator for photothermal ablation and as contrast agent for MRI were then evaluated, and promising results were obtained. They are capable of absorbing and efficiently converting NIR light into heat to generate thermoablative temperatures and cell lysis. They have potential for use as agents for T_2 MR contrast imaging and MR image-guided photothermal therapy. Last but not least, they can be magnetically manipulated in order to accumulate in a target site, to control their orientation, to improve cell uptake, to drive cell motion, and to trigger remote stirring in the biological environment.

products were washed four times with ethanol and chloroform, then centrifuged, followed by the conventional filtration method to remove NPs formed outside CNTs. For the synthesis of Co inside CNTs, the reaction was conducted under Ar atmosphere. These samples are denoted as $\text{Fe}_{3-x}\text{O}_4@\text{CNTs}$ and CoO@CNTs .

After this first filling step, once the mixture was heated and cooled to room temperature, the same synthesis was repeated again only with CNTs filled with iron oxide NPs without washing steps by adding either iron or cobalt stearate as a precursor. After this second step, the samples were denoted as $\text{Fe}_{3-x}\text{O}_4/\text{CoO@CNTs}$ and $\text{Fe}_{3-x}\text{O}_4/\text{Fe}_{3-x}\text{O}_4@\text{CNTs}$.

Characterization Techniques. Transmission electron microscopy was carried out using a JEOL 2100F (voltage 200 kV) microscope with a point resolution of 0.2 nm. The sample was dispersed in ethanol by ultrasonication during 5 min, and a drop of the solution was then deposited on a copper grid (covered with a carbon membrane).

X-ray diffraction (XRD) was carried out using a Bruker D8 Advance in the 27–75° (2θ) range with a scan step of 0.03°. The detector was a 3° wide analysis detector ("Lynx Eye"). Thermal gravimetric analyses were carried out with a TA Instrument (Q-5000 model). They were performed under an air flow up to 1000 °C with a heating rate of 5 °C/min. The concentrations of iron and cobalt metals in CNTs were determined by using a Spectro ARCOS ICP-AES. The samples were digested by boiling CNT suspensions in concentrated nitric acid (Sigma-Aldrich, trace metal basis grade) for 1 h, and the solutions were diluted with filtered ultrapure water for analysis.

Magnetization measurements were carried out with a Quantum Design MPMS QQUID-VSM magnetometer. Magnetization curves as a function of the applied magnetic field were measured at 400 and 5 K, sweeping the magnetic field from +7 T to -7 T and then from -7 T to +7 T.

Functionalization of Filled CNTs. All reagents and solvents were purchased from different commercial suppliers and used as received.

Arylation of Empty and Filled MWCNTs. To a suspension of CNTs (15 mg) dispersed in *o*-dichlorobenzene (25 mL) using a water bath sonication for 1 min was added a solution of Pht-protected 4-(aminomethyl)phenylamine derivative⁴⁸ (55 mg) in acetonitrile (4 mL). The mixture was sonicated in a water bath for 1 min. Argon was bubbled in the suspension for 15 min. Isoamyl nitrite (100 μL) was added, and the mixture was heated at 60 °C for 13 h. A solution of Pht-protected 4-(aminomethyl)phenylamine derivative (55 mg) in acetonitrile (4 mL) and isoamyl nitrite (100 μL) was then added at 60 °C, and the mixture was further heated at 60 °C for 4 h. After being cooled to room temperature, the suspension was filtered over a PTFE membrane (0.1 μm, Omnipore, Millipore). The solid recovered on the filter was dispersed in methanol (100 mL), sonicated for 1 min in a water bath, and filtered over a PTFE membrane (0.1 μm). This sequence was repeated with DMF, methanol, and dichloromethane. The resulting solid was dried under vacuum. The same procedure was repeated with the filled CNTs.

Pht Deprotection of Functionalized MWCNTs. To a suspension of functionalized CNTs (11 mg) in ethanol (11 mL) was added hydrazine hydrate (1.1 mL). The dispersion was sonicated in a water bath for 1 min and stirred for 14 h. The suspension was filtered over a PTFE (0.1 μm) membrane. The solid recovered on the filter was dispersed in DMF (100 mL), sonicated for 1 min in a water bath, and filtered over a PTFE membrane (0.1 μm). This sequence was repeated with methanol and dichloromethane. The resulting solid was dried under vacuum. The same procedure was repeated with the filled CNTs.

To assess the amount of amine functions on the CNTs, the Kaiser test was performed according to the procedure described in ref 48.

MRI Measurements. Magnetic resonance imaging was performed on a Bruker Bio-Spec 47/40 USR Scanner, a 40 cm bore actively shielded 4.7 T scanner equipped with a whole-volume radiofrequency (RF) coil in the Small Animal Imaging Platform Paris – Descartes PARCC-HEGP. The scanner was interfaced to ParaVision software for preclinical MRI research. Agarose gels (0.3%, 630 μL) containing CNTs at different concentrations up to 25 μg/mL were imaged using spin-echo sequences with different echo times (T_E) and repetition times (T_R) in order to deduce the longitudinal and transverse relaxation time, T_1 and T_2 , of proton magnetization.

Cell Experiments. Cell Culture and Exposition to CNT-NPs. SKOV3 human ovarian carcinoma cells were maintained as a monolayer culture in McCoy 5A culture Medium supplemented with 10% fetal bovine serum, 1% penicillin–streptomycin at 37 °C, and 5% of CO₂. Cells were incubated with Fe_{3-x}O₄/CoO@CNTs and Fe_{3-x}O₄/Fe_{3-x}O₄@CNTs in complete McCoy culture medium at concentrations of 5, 10, 20, and 50 μg/mL in different conditions: for 1 or 24 h without magnet or for 1 in the presence of a permanent magnet placed under the culture dish. After three rinsing steps with PBS, cells were observed by optical microscopy or prepared for further experiments.

Laser Irradiation and Thermographic Measurements. To quantify heat generation by Fe_{3-x}O₄/CoO@CNTs and Fe_{3-x}O₄/Fe_{3-x}O₄@CNTs, 50 μL of CNT suspension at concentrations of

200, 500, and 1000 μg/mL was irradiated in Eppendorf tubes using a 808 nm diode laser featuring a fiber delivery system (BWT) at a light fluence of 1, 2, or 4 W/cm². The temperature of the suspension was monitored using a FLIR SC7000 infrared camera. All the acquisitions were processed by Altair software (FLIR Systems, Inc.). Specific absorption rate (SAR) was deduced following the formula

$$\text{SAR} = \frac{C_{\text{water}} V_S}{m} \frac{dT}{dt}$$

where C_{water} is the volume-specific heat capacity of the water ($C_{\text{water}} = 4185 \text{ J} \cdot \text{L}^{-1} \cdot \text{K}^{-1}$), V_S is the volume of the suspension ($V_S = 50 \mu\text{L}$), m is the mass of CNTs, and dT/dt is the initial temperature gradient.

For cell irradiation, cell monolayers seeded in 12-well plates were labeled with Fe_{3-x}O₄/CoO@CNTs at concentrations of 10, 20, and 50 μg/mL for 1 h in the presence of the magnet or for 24 h without magnet. After three washing step with PBS, cells were exposed to the 808 nm diode laser (4 W/cm²) for 200 or 500 s.

Cell Viability Test. The cytotoxicity of CNTs labeling, magnetic stirring, and laser irradiation (IR) treatment was evaluated by AlamarBlue assay, which assesses the metabolic activity of cells. After labeling with CNTs and IR treatment (or magnetic stirring), the cells' monolayers were cultured overnight in complete medium and then incubated with an AlamarBlue solution (10%, Invitrogen) in culture medium for 2 h, following the protocol provided by the manufacturer. The fluorescence in cell medium due to the reduction of resazurin (oxidized form) to resorufin by cell activity was analyzed with a microplate reader (BMG Fluostar Galaxy), with an excitation wavelength of 550 nm, and by collecting the fluorescence at 590 nm. All the experimental points were performed in triplicate. Unlabeled SKOV3 cells were used as controls.

Electron Microscopy on Cells. For TEM localization of CNTs, SKOV3 cells were exposed to Fe_{3-x}O₄/CoO@CNTs (5 μg/mL) for 6 h at 37 °C with a magnetic field parallel or perpendicular to the cell layer. Following the incubation, cells were rinsed three times with PBS and fixed in presence of the magnetic field with 5% glutaraldehyde in 0.1 mol/L sodium cacodylate buffer. Cell were post fixed with 1% osmium tetroxide containing 1.5% potassium cyanoferrate, gradually dehydrated in increasing concentrations of ethanol and embedded in Epon resin. Thin sections (70 nm) of cells parallel to the cell layer were examined with a Zeiss EM 902 transmission electron microscope at 80 kV (platform MIMA2, INRA, Jouy-en-Josas, France). For scanning electron microscopy (SEM), cells were seeded on 12 mm diameter circular glass lamella. They were exposed to Fe_{3-x}O₄/CoO@CNTs (5 μg/mL) for 1 h (without magnet or with the magnet under the flask (magnetic field perpendicular to the cell layer). After incubation and washing, they were fixed using a glutaraldehyde solution (2.5% glutaraldehyde in 0.2 M sodium cacodylate buffer, pH 7.4) for 1 h at room temperature. The fixative was removed, and samples were rinsed three times for 10 min in the sodium cacodylate solution (pH 7.4). The samples underwent progressive dehydration by soaking in a graded series of ethanol (50–100%) before critical-point drying under CO₂. Samples were mounted on aluminum stubs (10 mm diameter) with conductive silver paint and sputter coated with gold–palladium (Polaron SC7640; Elexience, Verrières-le-buisson, France) for 200 s at 10 mA. Samples were visualized by field emission gun scanning electron microscopy. They were viewed as secondary electron images (2 kV) with a Hitachi S4500 instrument (Elexience, Verrières-le-buisson, France). Scanning electron microscopy analyses were performed at the Microscopy and Imaging Platform MIMA2 (Micalis, B2HM, Massy, France) of the INRA research center of Jouy-en-Josas (France).

Quantification of Cell Mobility and CNT Uptake by Single-Cell Magnetophoresis. To quantify the magnetophoretic mobility of labeled cells and the associated CNT load, cells were thoroughly washed after labeling and trypsinized to obtain a dilute suspension. The cell suspension was introduced in a quartz chamber and submitted to a magnet creating a magnetic field B of 150 mT and a uniform field gradient (grad B) of 17 T·m⁻¹. The cell motion toward the magnet was recorded by video-microscopy, as described previously.⁶² Under the experimental

conditions, the magnetic driving force acting on cells ($M \times \text{grad } B$, where M is the cell magnetic moment) is balanced by the viscous force ($3\pi\eta dv$, where d is the cell diameter, v is the cell velocity and η is the medium viscosity). The cell magnetization was thus deduced from the velocity and diameter of each cell. The magnetization and magnetic content of CNTs being calculated from elemental analysis and magnetic measurement, the amount of CNTs per cell could be deduced.

Magnetic Stirring Experiment. SKOV3 cells were labeled with $\text{Fe}_{3-x}\text{O}_4/\text{CoO}$ @CNTs (5 $\mu\text{g}/\text{mL}$) for 30 min and washed three times with PBS. Immediately after labeling, the adherent cells were exposed to a rotating magnetic field (1 Hz) in the plane parallel to the cell layer and recorded by videomicroscopy. The experimental set up to generate the rotating field under microscope has been described previously. The miniaturized magnetic device consists of two pairs of coils magnetizing two pairs of soft iron assembled perpendicularly and separated by only 0.6 mm. The magnetic field created in the center can be tuned between 0 to 70 mT and rotated in the cell layer plane when the two pairs of coils are supplied with an alternating current 90° out of phase.

Conflict of Interest: The authors declare no competing financial interest.

Acknowledgment. This work was supported by ANR P2N (NANOTHER project 2010-NANO-008-398 04), by CNRS, by the University of Strasbourg, and by the HINT MP1202 COST. We thank C. Péchoux and S. Chat for transmission electron microscopy of cells, T. Meylheuc for scanning electron microscopy, G. Autret, O. Clément, and J. Kolosnjaj for MRI experiments and image processing, R. Di Corato, C. Kiefer, A. Derori, and D. Burger for technical assistance, and I. A. Vacchi for preliminary experiments on CNT functionalization, and Patrice Flaud for infrared thermometry.

Supporting Information Available: Figures S1–S10. This material is available free of charge via the Internet at <http://pubs.acs.org>.

REFERENCES AND NOTES

- Laurent, S.; Forge, D.; Port, M.; Roch, A.; Robic, C.; Vander, E. L.; Muller, N. R. Magnetic Iron Oxide Nanoparticles: Synthesis, Stabilization, Vectorization, Physicochemical Characterizations, and Biological Applications. *Chem. Rev.* **2008**, *108*, 2064–2110.
- Molenbroek, A. M.; Helveg, S.; Topsøe, H.; Clausen, S. B. Nano-Particles in Heterogeneous Catalysis. *Top Catal.* **2009**, *52*, 1303–1311.
- Yin, Y.; Talapin, D. V. The Chemistry of Functional Nanomaterials. *Chem. Soc. Rev.* **2013**, *42*, 2484–2487.
- Sun, S.; Zheng, H. Size-Controlled Synthesis of Magnetite Nanoparticles. *J. Am. Chem. Soc.* **2002**, *124*, 8204–8205.
- Pichon, B. P.; Barbillon, G.; Marie, P.; Pauly, M.; Begin, C. S. Iron Oxide Magnetic Nanoparticles Used as Probing Agents to Study the Nanostructure of Mixed Self-Assembled Monolayers. *Nanoscale* **2011**, *3*, 4696–4705.
- Papaefthimiou, V.; Florea, I.; Baaziz, W.; Janowska, I.; Doh, W. H.; Begin, D.; Blume, R.; Knop-Gericke, A.; Ersen, O.; Pham-Huu, C.; et al. Effect of the Specific Surface Sites on the Reducibility of $\alpha\text{-Fe}_2\text{O}_3$ /Graphene Composites by Hydrogen. *J. Phys. Chem. C* **2013**, *117*, 20313–20319.
- Qu, Q.; Yang, S.; Feng, X. 2D Sandwich-like Sheets of Iron Oxide Grown on Graphene as High Energy Anode Material for Supercapacitors. *Adv. Mater.* **2011**, *23*, 5574–5580.
- Baaziz, W.; Phuoc, L. T.; Duong, C. V.; Melinte, G.; Janowska, I.; Ersen, O.; Zafeiratos, S.; Begin, D.; Begin, S. C.; Pham, C. H. Few Layer Graphene Decorated with Homogeneous Magnetic Fe_3O_4 Nanoparticles with Tunable Covering Densities. *J. Mater. Chem. A* **2014**, *2*, 2690–2700.
- Kim, I. T.; Magasinski, A.; Jacob, K.; Yushin, G.; Tannenbaum, R. Synthesis and Electrochemical Performance of Reduced Graphene Oxide/Maghemitite Composite Anode for Lithium Ion Batteries. *Carbon* **2013**, *52*, 56–64.
- Pankhurst, Q. A.; Connolly, J.; Jones, S. K.; Dobson, J. Applications of Magnetic Nanoparticles in Biomedicine. *J. Phys. Appl. Phys.* **2003**, *36*, R167–R181.
- Reddy, L. H.; Arias, J. L.; Nicolas, J.; Couvreur, P. Magnetic Nanoparticles: Design and Characterization, Toxicity and Biocompatibility, Pharmaceutical and Biomedical Applications. *Chem. Rev.* **2012**, *112*, 5818–5878.
- Kostarelos, K.; Bianco, A.; Prato, M. Promises, Facts and Challenges for Carbon Nanotubes in Imaging and Therapeutics. *Nat. Nanotechnol.* **2009**, *4*, 627–633.
- Hong, H.; Gao, T.; Cai, W. Molecular Imaging with Single-walled Carbon Nanotubes. *Nano Today* **2009**, *4*, 252–261.
- Kim, J. W.; Galanatha, E. I.; Shashkov, E. V.; Moon, H. M.; Zharov, V. P. Golden Carbon Nanotubes as Multimodal Photoacoustic and Photothermal High-Contrast Molecular Agents. *Nat. Nanotechnol.* **2009**, *4*, 688–694.
- Welsher, K.; Liu, Z.; Sherlock, S. P.; Robinson, J. T.; Chen, Z.; Daranciang, D.; Dai, H. A Route to Brightly Fluorescent Carbon Nanotubes for Near-infrared Imaging in Mice. *Nat. Nanotechnol.* **2009**, *4*, 773–780.
- Lamanna, G.; Garofalo, A.; Popa, G.; Wilhelm, C.; Begin, S. C.; Flesch, D. F.; Bianco, A.; Gazeau, F.; Moyon, M. C. Endowing Carbon Nanotubes with Superparamagnetic Properties: Applications for Cell Labeling, MRI Cell Tracking and Magnetic Manipulations. *Nanoscale* **2013**, *5*, 4412–4421.
- Delogu, L. G.; Vidili, G.; Venturelli, E.; Ménard-Moyon, C.; Zoroddu, M. A.; Pilo, G.; Nicolussi, P.; Ligios, C.; Bedognetti, D.; Sgarrella, F.; et al. Functionalized Multiwalled Carbon Nanotubes as Ultrasound Contrast Agents. *Proc. Natl. Acad. Sci. U.S.A.* **2012**, *109*, 16612–16617.
- Wang, C.; Ma, X.; Ye, S.; Cheng, L.; Yang, K.; Guo, L.; Li, C.; Li, Y.; Liu, Z. Protamine Functionalized Single-Walled Carbon Nanotubes for Stem Cell Labeling and *in Vivo* Raman/Magnetic Resonance/Photoacoustic Triple-Modal Imaging. *Adv. Funct. Mater.* **2012**, *22*, 2363–2375.
- Singh, R.; Torti, S. V. Carbon Nanotubes in Hyperthermia Therapy. *Adv. Drug Delivery Rev.* **2013**, *65*, 2045–2060.
- Shen, S.; Kong, F.; Guo, X.; Wu, L.; Shen, H.; Xie, M.; Wang, X.; Jin, Y.; Ge, Y. CMCTS Stabilized Fe_3O_4 Particles with Extremely Low Toxicity as Highly Efficient Near-infrared Photothermal Agents for *in Vivo* Tumor Ablation. *Nanoscale* **2013**, *5*, 8056–8066.
- Liu, X.; Tao, H.; Yang, K.; Zhang, S.; Lee, S. T.; Liu, Z. Optimization of Surface Chemistry on Single-Walled Carbon Nanotubes for *in Vivo* Photothermal Ablation of Tumors. *Biomaterials* **2011**, *32*, 144–151.
- Wu, H.; Liu, G.; Zhuang, Y.; Wu, D.; Zhang, H.; Yang, H.; Hu, H.; Yang, S. The Behavior after Intravenous Injection in Mice of Multiwalled Carbon Nanotube/ Fe_3O_4 Hybrid MRI Contrast Agents. *Biomaterials* **2011**, *32*, 4867–4876.
- Wang, J. T. W.; Cabana, L.; Bourgognon, M.; Kafa, H.; Protti, A.; Venner, K.; Shah, A. M.; Sosabowski, J. K.; Mather, S. J.; Roig, A.; et al. Magnetically Decorated Multiwalled Carbon Nanotubes as Direct MRI and SPECT Contrast Agent. *Adv. Funct. Mater.* **2014**, *24*, 1880–1894.
- Tessonniere, J. P.; Rosenthal, D.; Girgsdies, F.; Amadou, J.; Bégin, D.; Pham-Huu, C.; Su, S. D.; Schlägl, R. Influence of the Graphitisation of Hollow Carbon Nanofibers on Their Functionalisation and Subsequent Filling with Metal Nanoparticles. *Chem. Commun.* **2009**, *46*, 7158–7160.
- Castillejos, E.; Deboutiere, P. J.; Roiban, L.; Solhy, A.; Martinez, V.; Kihn, Y.; Ersen, O.; Philippot, K.; Chaudret, B.; Serp, P. An Efficient Strategy to Drive Nanoparticles into Carbon Nanotubes and the Remarkable Effect of Confinement on Their Catalytic Performance. *Angew. Chem., Int. Ed.* **2009**, *48*, 2529–2533.
- Baaziz, W.; Begin, S.; Pichon, B. P.; Florea, I.; Ersen, O.; Zafeiratos, S.; Barbosa, R.; Begin, D.; Pham-Huu, C. High-Density Mono-dispersed Cobalt Nanoparticles Filled into Multiwalled Carbon Nanotubes. *Chem. Mater.* **2012**, *24*, 1549–1551.
- Baaziz, W.; Liu, X.; Florea, I.; Begin, S.; Pichon, B. P.; Ulhaq, C.; Ersen, O.; Soria, S. M.; Zafeiratos, S.; Janowska, I.; et al. Carbon Nanotube Channels Selectively Filled with Mono-dispersed $\text{Fe}_{3-x}\text{O}_4$ Nanoparticles. *J. Mater. Chem. A* **2013**, *1*, 13853–13861.
- Bao, J.; Tie, C.; Xu, Z.; Suo, Z.; Zhou, Q.; Hong, J. A Facile Method for Creating an Array of Metal-Filled Carbon Nanotubes. *Adv. Mater.* **2002**, *14*, 1483–1486.

29. Hampel, S.; Leonhardt, A.; Selbmann, D.; Biedermann, K.; Elefant, D.; Müller, Ch.; Gemming, T.; Büchner, B. Growth and Characterization of Filled Carbon Nanotubes with Ferromagnetic Properties. *Carbon* **2006**, *44*, 2316–2322.

30. Leonhardt, A.; Haampel, S.; Müller, C.; Mönch, I.; Koseva, R.; Ritschel, M.; Elefant, D.; Biedermann, K.; Büchner, B. Synthesis, Properties, and Applications of Ferromagnetic-Filled Carbon Nanotubes. *Chem. Vap. Deposition* **2006**, *12*, 380–387.

31. Gui, X.; Wei, J.; Wang, K.; Wang, W.; Lv, R.; Chang, J.; Kang, F.; Gu, J.; Wu, D. Improved Filling Rate and Enhanced Magnetic Properties of Fe-filled Carbon Nanotubes by Annealing and Magnetic Separation. *Mater. Res. Bull.* **2008**, *43*, 3441–3446.

32. Korneva, G.; Ye, H.; Gogotsi, Y.; Halverson, D.; Friedman, G.; Bradley, J. C.; Kornev, K. Carbon Nanotubes Loaded with Magnetic Particles. *Nano Lett.* **2005**, *5*, 879–884.

33. Kopyl, S.; Bystrov, V.; Bdikin, I.; Maiorov, M.; Sousa, A. C. M. Filling Carbon Nanotubes with Magnetic Particles. *J. Mater. Chem. C* **2013**, *1*, 2860–2866.

34. Ersen, O.; Bégin, S.; Houllé, M.; Amadou, J.; Janowska, I.; Grenèche, J. M.; Crucifix, C.; Pham-Huu, C. Microstructural Investigation of CoFe_2O_4 Nanowires Inside Carbon Nanotubes by Electron Tomography. *Nano Lett.* **2008**, *8*, 1033–1040.

35. Belesi, M.; Philippe, T.; Rouschatzakis, I.; Wu, H. C.; Berger, H.; Granville, S.; Shvets, I. V.; Ansermet, J.-Ph. Magnetic Properties of the Magnetoelectric Compound Cu_2OSeO_3 : Magnetization and ^{77}Se NMR Study. *J. Physics: Conf. Ser.* **2011**, *303*, No. 012069.

36. Yu, W. J.; Hou, P. X.; Li, F.; Liu, C. Improved Electrochemical Performance of Fe_2O_3 Nanoparticles Confined in Carbon Nanotubes. *J. Mater. Chem.* **2012**, *22*, 13756–13763.

37. Tessonner, J. P.; Ersen, O.; Weinberg, G.; Pham, H. C.; Su, D. S.; Schlögl, R. Selective Deposition of Metal Nanoparticles Inside or Outside Multiwalled Carbon Nanotubes. *ACS Nano* **2009**, *6*, 2081–2089.

38. Costa, P. M. F. J.; Sloan, J.; Rutherford, T.; Green, M. L. H. Encapsulation of Re_xO_y Clusters within Single-Walled Carbon Nanotubes and Their in Tubulo Reduction and Sintering to Re Metal. *Chem. Mater.* **2005**, *17*, 6579–6582.

39. Meng, L.; Chen, W.; Tan, Y.; Zou, L.; Chen, C.; Zhou, H.; Peng, Q.; Li, Y. Fe_3O_4 Octahedral Colloidal Crystals. *Nano Res.* **2011**, *4*, 370–374.

40. Baaziz, W.; Pichon, B. P.; Lefevre, C.; Bouillet, U. C.; Gneche, J. M.; Toumi, M.; Mhiri, T.; Bégin, C. S. High Exchange Bias in $\text{Fe}_{3-x}\text{O}_4@\text{CoO}$ Core Shell Nanoparticles Synthesized by a One-Pot Seed-Mediated Growth Method. *J. Phys. Chem. C* **2013**, *117*, 11436–11443.

41. Leighton, C.; Nogues, J.; Jonsson-Akerman, B. J.; Schuller, I. K. Coercivity Enhancement in Exchange Biased Systems Driven by Interfacial Magnetic Frustration. *Phys. Rev. Lett.* **2000**, *84*, 3466–3469.

42. Cheon, J.; Park, J. I.; Choi, J. S.; Jun, Y. W.; Kim, S.; Kim, M. G.; Kim, Y. M.; Kim, Y. J. Magnetic Superlattices and Their Nanoscale Phase Transition Effects. *Proc. Natl. Acad. Sci. U.S.A.* **2006**, *103*, 3023–3027.

43. Song, Q.; Zhang, Z. J. Controlled Synthesis and Magnetic Properties of Bimagnetic Spinel Ferrite CoFe_2O_4 and MnFe_2O_4 Nanocrystals with Core–Shell Architecture. *J. Am. Chem. Soc.* **2012**, *134*, 10182–10190.

44. Demortière, A.; Panissod, P.; Pichon, B.; Pourroy, G.; Guillou, D.; Donnio, B.; Bégin, C. S. Size-Dependent Properties of Magnetic Iron Oxide Nanocrystals. *Nanoscale* **2011**, *3*, 225–232.

45. Baaziz, W.; Pichon, B.; Fleutot, S.; Liu, Y.; Lefevre, C.; Gneche, J. M.; Toumi, M.; Mhiri, T.; Bégin, C. S. Magnetic Iron Oxide Nanoparticles: Reproducible Tuning of the Size and Nanosized-Dependent Composition, Defects, and Spin Canting. *J. Phys. Chem. C* **2014**, *118*, 3795–3810.

46. Pallai, V.; Shah, D. O. Synthesis of High-Coercivity Cobalt Ferrite Particles Using Water-in-oil Water Microemulsions. *J. Magn. Magn. Mater.* **1996**, *163*, 243–258.

47. Bahr, J. L.; Tour, J. M. Highly Functionalized Carbon Nanotubes Using *in Situ* Generated Diazonium Compounds. *Chem. Mater.* **2001**, *13*, 3823–3824.

48. Ménard, M. C.; Fabbro, C.; Prato, M.; Bianco, A. One-Pot Triple Functionalization of Carbon Nanotubes. *Chem.—Eur. J.* **2011**, *17*, 3222–3227.

49. Kaiser, E.; Colescott, R. L.; Bossinger, C. D.; Cook, P. I. Color Test for Detection of Free Terminal Amino Groups in the Solid-Phase Synthesis of Peptides. *Anal. Biochem.* **1970**, *34*, 595–598.

50. Samori, C.; Sainz, R.; Ménard, M. C.; Toma, F. M.; Venturelli, E.; Singh, P.; Ballestrini, M.; Prato, M.; Bianco, A. Potentiometric Titration as a Straightforward Method to Assess the Number of Functional Groups on Shortened Carbon Nanotubes. *Carbon* **2010**, *48*, 2447–2454.

51. Gillis, P.; Moiny, F.; Brooks, R. A. On T2-shortening by Strongly Magnetized Spheres: A Partial Refocusing Model. *Magn. Reson. Med.* **2002**, *47*, 257–263.

52. Perez, J. M.; Josephson, L.; O'Loughlin, T.; Hogemann, D.; Weissleder, R. Magnetic Relaxation Switches Capable of Sensing Molecular Interactions. *Nat. Biotechnol.* **2002**, *20*, 816–820.

53. Vuong, Q. L.; Berret, J. F.; Fresnais, J.; Gossuin, Y.; Sandre, O. A Universal Scaling Law to Predict the Efficiency of Magnetic Nanoparticles as MRI T2-Contrast Agents. *Adv. Healthcare Mater.* **2012**, *1*, 502–512.

54. Park, J. H.; von Maltzahn, G.; Zhang, L.; Schwartz, M. P.; Ruoslahti, E.; Bhatia, N. S.; Sailor, M. J. Magnetic Iron Oxide Nanoworms for Tumor Targeting and Imaging. *Adv. Mater.* **2008**, *20*, 1630–1635.

55. Yin, M.; Wang, M.; Miao, F.; Ji, Y.; Tian, Z.; Shen, H.; Jia, N. Water-Dispersible Multiwalled Carbon Nanotube/Iron Oxide Hybrids as Contrast Agents for Cellular Magnetic Resonance Imaging. *Carbon* **2012**, *50*, 2162–2170.

56. Liu, Y.; Hughes, T. C.; Muir, B. W.; Waddington, L. J.; Gengenbach, T. R.; Easton, C. D.; Hinton, T. M.; Moffat, B. A.; Hao, X.; Qiu, J. Water-Dispersible Magnetic Carbon Nanotubes as T2-Weighted MRI Contrast Agents. *Biomaterials* **2014**, *35*, 378–386.

57. Ding, X.; Singh, R.; Burke, A.; Hatcher, H.; Olson, J.; Kraft, R. A.; Schmid, M.; Carroll, D.; Bourland, J. D.; Akman, S.; et al. Development of Iron-Containing Multiwalled Carbon Nanotubes for MR-guided Laser-induced Thermotherapy. *Nanomedicine (London)* **2011**, *6*, 1341–1352.

58. Paquet, C.; de Haan, H. W.; Leek, D. M.; Lin, H. Y.; Xiang, B.; Tian, G.; Kell, A.; Simard, B. Clusters of Superparamagnetic Iron Oxide Nanoparticles Encapsulated in a Hydrogel: a Particle Architecture Generating a Synergistic Enhancement of the T2 Relaxation. *ACS Nano* **2011**, *5*, 3104–3112.

59. Park, J. H.; von Maltzahn, G.; Zhang, L.; Schwartz, M. P.; Ruoslahti, E.; Bhatia, N. S.; Sailor, J. M. Magnetic Iron Oxide Nanoworms for Tumor Targeting and Imaging. *Adv. Mater.* **2008**, *20*, 1630–1635.

60. Lartigue, L.; Hugounenq, P.; Alloyeau, D.; Clarke, S. P.; Lévy, M.; Bacri, J. C.; Bazzi, R.; Brougham, D. F.; Wilhelm, C.; Gazeau, F. Cooperative Organization in Iron Oxide Multi-Core Nanoparticles Potentiates Their Efficiency as Heating Mediators and MRI Contrast Agents. *ACS Nano* **2012**, *6*, 10935–10949.

61. Liu, D.; Wang, L.; Wang, Z.; Cuschieri, A. Magnetoporation and Magnetolysis of Cancer Cells via Carbon Nanotubes Induced by Rotating Magnetic Fields. *Nano Lett.* **2012**, *12*, 5117–5121.

62. Wilhelm, C.; Gazeau, F.; Bacri, J. C. Magnetophoresis and Ferromagnetic Resonance of Magnetically Labeled Cells. *Eur. Biophys. J.* **2002**, *31*, 118–125.